

A computational fluid dynamics investigation of fluid flow in a dense medium plasma reactor

Derek C Johnson^{1,3} and David S Dandy²

¹ Department of Chemistry, Colorado State University, Fort Collins, CO 80523, USA

² Department of Chemical & Biological Engineering, Colorado State University, Fort Collins, CO 80523, USA

E-mail: djohnson@engr.colostate.edu

Received 26 May 2006, in final form 12 October 2006

Published 5 January 2007

Online at stacks.iop.org/JPhysD/40/488

Abstract

Computational fluid dynamics are applied to the study of three-dimensional fluid flow in a dense medium plasma reactor (DMPR) under different operating conditions. Reaction mechanisms and rates for the removal of methyl *t*-butyl ether (MTBE) in a DMPR are developed from experimental data to determine the plasma volume, the rate of interphase mass transfer and the photolysis rate of MTBE via UV emission from the plasma. The simulations utilize the plasma volume determined from the kinetic data to show that the volume of fluid in contact with the plasma in the DMPR only constitutes a maximum of approximately 10% of the fluid intended to be cycled through the plasma tubules. The simulations also predict appreciable pressure gradients on the surface of the pin electrodes, resulting in a small discharge area located away from the region in which the electric field strength is a maximum. This result has been confirmed indirectly through observation in that the pin electrodes sputter metal from an area of similar size and location to the low-pressure region predicted by the simulations. The pressure gradients are shown to be a function of operating conditions as well as pin location, indicating that the plasma discharge conditions are not uniform throughout the reactor.

 Supplementary information, including additional figures, is available in the online edition at stacks.iop.org/jphysd/40/488.

1. Introduction

An increased awareness of the adverse effects of biological and chemical contamination on human health and the environment has motivated significant research in pollution prevention and remediation. This issue has prompted investigations into the disinfection of contaminated water and the removal of organic carbon by thermal and non-thermal plasmas. Plasma treatment is an appealing method due to its ability to simultaneously disinfect aqueous solutions and oxidize organic compounds. The process is characterized by the production of high oxidation potential species and a wide spectral emission. The UV radiation and oxidation species

produced by the plasma discharge are effective in deactivating microbial species, as well as initiating oxidation reactions. Due to these characteristics, plasma treatment is considered to be a promising alternative to current biological treatment methods, which reduce organic carbon, and disinfection processes such as chlorination, ozonation and UV lamps.

Numerous investigators have carried out experiments utilizing point-to-plane plasma discharge reactors for organic oxidation and microbial inactivation. Of these studies, two reactor configurations dominate the literature: (1) pin electrodes discharging in the gas phase above a solution [1–4] and (2) a point-to-plane electrode configuration submerged in an aqueous solution [5–19]. The first configuration results in a large production rate of gas phase oxidants such as $\cdot\text{OH}$, O_3 ,

³ Author to whom any correspondence should be addressed.

$\cdot\text{O}$, $\cdot\text{HO}_2$ and O_2^- . The molar density and spatial distribution of the oxidants can be controlled by manipulating the discharge atmosphere to contain large H_2O and O_2 partial pressures. The reaction and disinfection rates in this reactor configuration are, however, controlled by mass transfer and not reaction kinetics, resulting in pseudo first-order attenuation rates of a pollutant molecule. Thus, the oxidation of organic contaminants and inactivation of microbes in the aqueous solution is hindered by the diffusion rates of the oxidizing species across the gas–liquid interface and into the bulk liquid. Another consequence of generating a plasma discharge in an atmosphere above the liquid solution is that the oxidation and disinfection processes proceed solely by reaction with solvated oxidizing species. This is due to the fact that neither the organic molecules nor the microorganisms come into contact with the plasma, thereby eliminating interactions with high-energy electrons. The effect of losing this reaction pathway, with respect to organic oxidation, is that although the original organic contaminant is typically attenuated faster due to the large concentration of ozone produced by the discharge when compared with the second reactor configuration, the carbon is still in solution in the form of oxidation products. Thus, the total organic carbon (TOC) reduction rate is lower in this reactor configuration and can become negligible if the oxidation products are resistant to attack by the species produced by the plasma, requiring additional treatment methods to completely mineralize the organic carbon. In the case of microbial inactivation, plasma treatment is more effective when the microbes come into direct contact with the plasma. Another problem inherent to this design is that it presents scale up difficulties and is normally a batch or semi-batch process.

In the second reactor configuration, high potential oxidizing species such as $\cdot\text{OH}$, H_2O_2 , $\cdot\text{O}$, $\cdot\text{HO}_2$, O_2^- and O_3 (if O_2 is bubbled into the system) are also produced. However, the reaction and disinfection rates are still controlled by mass transfer and large plasma volumes can be difficult to sustain. As a result, the fluid volume in which oxidation reactions and microbial inactivation occur consists of a thin film surrounding the plasma arc tubule. Thus, while the reaction rate is not controlled by mass transfer rates across a gas–liquid interface, the rate is suppressed because the organic species and microbes must be transported, typically by diffusion, from the bulk solution to the plasma–liquid interface. Electron-impact dissociation reactions and microbial interactions with high-energy electrons are viable pathways in this reactor configuration, giving it an additional oxidation and disinfection route for which the rate is not a function of the contaminant species characteristics, and thus is not subject to the mineralization limitations prevalent in the first configuration. While the attenuation of the original organic contaminant is consistently slower when compared with the gas phase discharge configuration, the TOC concentration is reduced at a higher rate. However, this design also presents scale up difficulties. The first attempt to address issues inherent in these two configurations was the development of the dense medium plasma reactor (DMPR) by Denes and coworkers [20, 21].

2. Dense medium plasma reactor

The DMPR was developed by Denes and coworkers [20, 21] for reacting liquid/vapour phase species in an induced plasma

state using low temperature plasma chemistry. The reactor consists of a vessel containing a rotating array of 25 pin electrodes, stationary lower electrode, cooling system and gas introduction and discharge ports. The rotating pin array is intended to spatially homogenize the multiple arc discharges from the pin electrodes and to activate a larger effective volume of fluid. Spinning the pin array also pumps fresh liquid and gas into the discharge zone, thus thinning the boundary layer between the emission tips and the bulk fluid. Although the actual mechanism for electron emission and energy transport through the liquid is not well characterized, the rotation of the pin array acts as a field emission arc source, thereby generating numerous arc tubules originating from the pin electrode surfaces. Reactive or inert gases can also be introduced into the reactor to influence the plasma chemistry and reduce the applied potential required to initiate the formation of the arc tubules. A detailed schematic of the reactor and operating procedures can be found in [20–24].

The DMPR has been investigated as a tool for the disinfection of microbial contaminated water. Experiments conducted by Manolache *et al* [22] focused on quantifying the inactivation of specific bacteria and the mechanisms responsible for the disinfection. The oxidation of methyl *t*-butyl ether (MTBE) and subsequent formation of oxidation products in a DMPR have also been explored [24]. The experiments were designed to study MTBE oxidation mechanisms and examine possible operating conditions that promote the complete oxidation of the contaminant molecule to carbon dioxide. The MTBE oxidation experiments utilized two reactor configurations denoted original and coaxial. The original configuration is the DMPR as described above when oxygen is injected into the system through the middle of the stationary electrode. A nebulizer has been added to the original reactor configuration, allowing the liquid and oxygen to be transported coaxially through the middle of the stationary electrode to the reaction zone. This arrangement ensured that the solution in the reaction zone would be saturated with oxygen and that oxygen bubble surface area would be maximized. This reactor configuration is referred to as the coaxial configuration, while an aqueous discharge without a nebulizer or coaxial flow is called the original configuration. These configurations are discussed in more detail in Johnson *et al* [24] and a diagram of the reactor and its two configurations is also contained in supplementary figure S1. The DMPR has also been applied to the oxidation of aqueous benzene, toluene, ethylbenzene, *m*- and *p*-xylene and *o*-xylene [23]. Those experiments also demonstrated the ability of the reactor to attenuate contaminant levels below drinking water standards on the order of minutes for small solution volumes.

While the oxidation experiments performed in the DMPR showed promise, deviations from the original hypothesis—reaction kinetics dominated by oxidation initiated by reactive species such as hydroxyl radical—resulted in additional questions concerning the reaction and plasma discharge mechanisms. The experiments performed by Johnson *et al* [24] demonstrated that if the original contaminant molecule was volatile enough to be promoted to the gas phase, and thus enveloped by the plasma, significant quantities of the initial organic carbon were completely oxidized to carbon dioxide in the DMPR. To enhance the amount of contaminant undergoing

complete oxidation of vapour phase organics to carbon dioxide in the plasma stream, convective and diffusive mechanisms are employed in the DMPR to promote the transport of the contaminant species from the bulk solution to the plasma. The pin array was spun at rates higher than 500 rpm, increasing convective mass transfer through turbulent mixing effects. However, the volume of contaminated liquid transformed into the plasma cannot be determined experimentally, and thus the efficiency of the reactor, as measured by the cycling of the bulk liquid to the plasma, is not known. It is also observed experimentally that the plasma discharge initiates from a specific region of the pin electrode surface that does not correspond to the point for which the radius of curvature is minimized. This result is inconsistent with the fact that a lower radius of curvature in a point-to-plane electrode configuration yields a higher electric field strength, and thus should be the surface position for which the plasma discharge is initiated. In the DMPR, however, the discharges occur along the rear (downstream) surfaces of the pin electrodes. These observations lead to additional questions concerning the character of the velocity field and fluid properties, but the design of the DMPR and the nature of the treatment process make it impossible to experimentally investigate the deviations from the original hypothesis. To investigate these very important issues, a rigorous computational fluid dynamics (CFD) approach is used.

CFD simulations are singularly suited to provide qualitative and quantitative information, which may not be readily accessible in the experiments, regarding the interaction of the liquid in the DMPR with the plasma and the characterization of the fluid in the vicinity of the plasma. The simulations are utilized to provide insight into the following questions that arose as a consequence of experimental results: (1) what is the volumetric flow rate of the liquid through the plasma as a function of pin array spin rate and reactor configuration? and (2) does spinning the pin array induce a pressure gradient along the surface of the pin electrodes, thus focusing the location of the discharge to a distinct region on the pin electrode surface away from the location where the radius of curvature is minimized?

Before the CFD simulations may be carried out, it is necessary to determine the plasma volume, which can be calculated from the data provided from a detailed kinetic analysis of the reactor. While the experiments performed by Johnson *et al* [24] and Manolache *et al* [23] yielded data that were well described by a pseudo first-order rate equation, shown in figure 1, the fits were empirical and do not capture the individual attenuation mechanisms. Thus, a more detailed analysis of the kinetic data and possible removal mechanisms are required to determine the parameters necessary to perform the CFD simulations.

3. Kinetic analysis

Four rate processes must be considered when performing a material balance on a chemical species in the DMPR—accumulation, convective mass transfer, diffusion and sources and/or sinks due to physical and chemical mechanisms. The dimensional form of the species conservation equation is

$$\frac{\partial C_i}{\partial t} + \mathbf{v} \cdot \nabla C_i = D_{i_{\text{mix}}} \nabla^2 C_i + r_i, \quad (1)$$

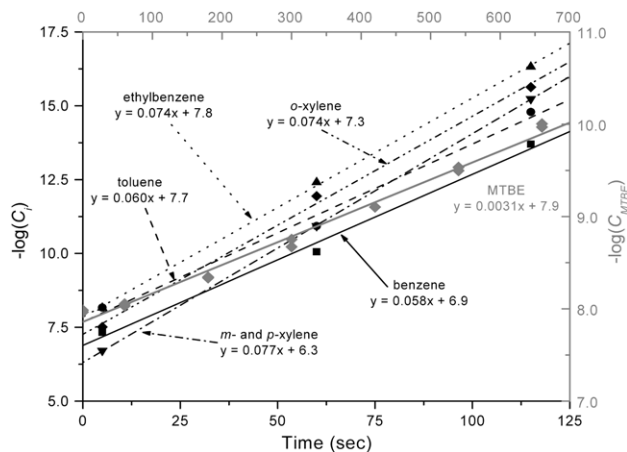


Figure 1. Plots of the $-\log(C_i)$ versus time for benzene (■), ethylbenzene (▲), toluene (●), *m*- and *p*-xylene (▼), and *o*-xylene (◆) in an originally configured DMPR. The right vertical and top horizontal axis dictate the $-\log(C_{\text{MTBE}})$ versus time data (◆) in an originally configured DMPR. Different scales are needed due to the length of the MTBE oxidation experiments. First-order fits to the experimental data are also included.

where \mathbf{v} is the local velocity vector, $D_{i_{\text{mix}}}$ is the diffusion coefficient for species i in the mixture, and r_i is the net production rate of species i (which in this case is negative for the original contaminant molecule) by a series of homogenous reactions. Equation (1) is a microscopic balance that cannot be solved until additional chemical kinetic information is obtained from a macroscopic balance. Considering that the DMPR is operated in a batch configuration, i.e. a closed system, the macroscopic species conservation equation reduces to the following ideal batch reactor design equation:

$$\frac{\partial C_i}{\partial t} = r_i. \quad (2)$$

The sources and sinks of species i in the DMPR are the result of a number of physical and chemical processes. The chemical mechanisms may be further divided into localized and extended effects, depending on the region over which the reactions occur [6]. Local effects are defined as those that occur in the immediate vicinity of the plasma. These effects include oxidation within the plasma tubules resulting from interactions with energetic electrons. Additionally, there are reactions with radicals and other highly reactive species in a region of hot gas adjacent to the plasma tubules that is not in thermal equilibrium with the plasma [25]. Radicals and other reactive species are formed in this region of hot gas by photolysis and dissociation of water molecules. Photolysis occurs from vacuum ultraviolet (VUV) radiation produced by the plasma discharge, and the dissociation reactions are caused by the impact of electrons accelerated into the plasma–water interface by the strong electric field produced in the reactor. These processes complement one another to degrade a variety of organic contaminants and are also effective for sterilization. The extended effects of the plasma discharge in the DMPR are considered to be those occurring outside the plasma channel and are principally due to the UV radiation propagating into the bulk solution [16]. The UV radiation can cause the photo-initiated oxidation of organic species.

As for the physical mechanisms, if a species is volatile, interphase mass transfer may be an important removal process and must be included. If interphase mass transfer is the lone physical removal mechanism, the rate at which species i is removed from the DMPR can be expressed as

$$(r_i)_{\text{mt}} = - \left(\frac{A_I D_{i,\text{mix}}}{V_L \delta} \right) C_i = -k_{\text{mt}} C_i, \quad (3)$$

where A_I is the interfacial area, V_L is the volume of the liquid, $D_{i,\text{mix}}$ is the diffusion coefficient for species i in the mixture and δ is the film thickness [24]. Equation (3) assumes that the mass transfer rate is low and thus the overall mass transfer rate coefficient k_{mt} is not a function of C_i . To check the validity of this assumption, finite difference methods are used to approximate the derivative of C_{MTBE} with respect to time from the interphase mass transfer control experiment data. The log of the negative derivative is plotted versus the log of C_{MTBE} to determine the order of the interphase mass transfer rate. The finite difference analysis yields a slope of 2.05 with an R^2 value (i.e. the statistical correlation of the data to a linear least squares analysis) of 0.87. Thus, the k_{mt} needs to be corrected for the dependence of the coefficient on the transfer of mass across the interface [26]. To account for this dependence, linear and quadratic terms are included in the mass transfer rate expression while higher order terms in the series are truncated. This is consistent with the Burnett equations that result from expressing molecular fluxes in terms of the first and second spatial derivatives of species molar density and the square of the first spatial derivative of species molar density [27]. Performing nonlinear least squares analysis on the expression containing first and second-order terms yields a linear coefficient that is five orders of magnitude smaller than the quadratic coefficient and results in a R^2 value significantly lower than the R^2 value obtained from the expression that contains only the quadratic term. Based on the above analysis, it is concluded that the overall mass transfer coefficient in equation (3) is linearly dependent on the molar density of MTBE. To remove the dependence from the coefficient, the interphase mass transfer rate is deduced to be second order, resulting in the following functional form for the rate of interphase mass transfer in the DMPR when employing operating conditions utilized by Johnson *et al* [24].

$$(r_i)_{\text{mt}} = \left(\frac{dC_i}{dt} \right)_{\text{mt}} = -k_{\text{mt}} C_i^2. \quad (4)$$

The average concentration of species i in the DMPR as a function of time when oxygen is introduced into the system without initiating a plasma discharge can then be determined by solving equation (4) and is

$$\frac{C_{i_0}}{C_i} = 1 + C_{i_0} k_{\text{mt}} t. \quad (5)$$

Data for the sparging of MTBE in the original and coaxial configurations of the DMPR are presented in figure 2. The plot illustrates the second-order loss of MTBE due to interphase mass transfer as a function of time. The loss rate in the coaxial configuration is approximately 50% greater than in the original configuration. This increase may be attributed to the installation of a nebulizer. Although the gas flow rate into

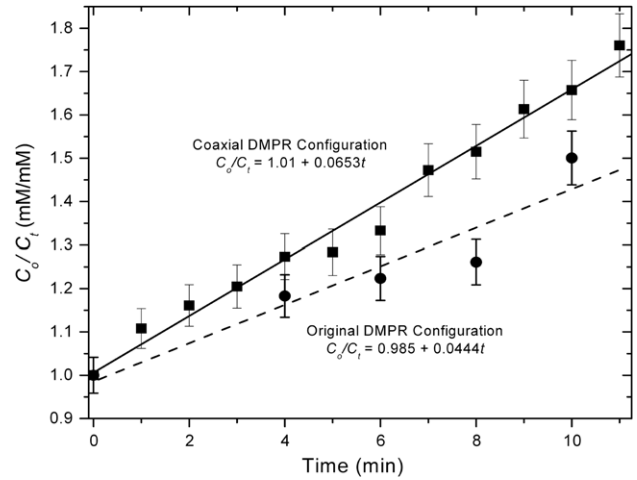


Figure 2. A plot of the inverse normalized MTBE concentration as a function of time for an originally (●) and coaxially (■) configured DMPR. The data represents the contribution of interphase mass transfer to the overall attenuation of MTBE, which is plotted in figure 1. The slope of the linear fits can be used to calculate the second-order interphase mass transfer rate coefficient, k_{mt} .

the system remains constant, the nebulizer produces bubbles with a smaller diameter when compared with the bubbles generated without the nebulizer in the original configuration, therefore increasing the interfacial area. While the above approach removes the concentration dependence of k_{mt} when the plasma is absent, the rate of interphase mass transfer will decrease as oxidation occurs as a result of the discharge. Thus, the second-order loss process and the interphase mass transfer rate coefficient calculated are used as starting points when modelling the combined loss processes present in the DMPR. While the removal of a species by sparging can be an important process in the DMPR, removal mechanisms due to localized and extended effects of the plasma discharge also contribute to the attenuation of the original contaminant.

When evaluating the chemical removal mechanisms associated with extended effects, direct photolysis should be considered. The relation of the time dependence on the concentration of species i due to oxidation initiated by direct photolysis is

$$(r_i)_{\text{DP}} = -\phi(\lambda) I_o(\lambda, t) \{1 - \exp(-2.303 \varepsilon \ell C_i)\}, \quad (6)$$

where $\phi(\lambda)$ is the photolysis quantum yield, $I_o(\lambda, t)$ is the UV intensity, ε is the extinction coefficient and ℓ is the path length [6, 19]. The DMPR produces a continuous plasma discharge that emits a broad radiation spectrum, which removes the time and wavelength dependence from the expression. Also, in an aqueous solution, the extinction coefficient is sufficiently large that the exponential term becomes negligible. Thus, the rate of change of the concentration of species i in the DMPR due to direct photolysis can be written as

$$(r_i)_{\text{DP}} = -\phi I_o = -k_{\text{DP}}, \quad (7)$$

where k_{DP} is a zero-order rate constant associated with direct photolysis. Finally, the attenuation of species i due to the plasma must be explored to completely describe the removal mechanisms associated with the DMPR.

An aqueous organic species transferred into the plasma may undergo either electron-impact dissociation reactions or oxidation initiated by hydrogen abstraction reactions with oxidizing species produced by the discharge. If the solution is well mixed, as in the DMPR, the measured concentration of the pollutant for a pulsed discharge reactor after one discharge is

$$C_i = \left(\frac{V_T + V_p}{V_T} \right) C_{i_0}, \quad (8)$$

where V_T and V_p are the volumes of the solution and plasma, respectively [6, 19]. The expression can be extended to N total discharges, yielding the following result:

$$C_{i_N} = \left(\frac{V_T + V_p}{V_T} \right) C_{i_{N-1}}. \quad (9)$$

While the DMPR has an intrinsic time constant (α) associated with the duration of the plasma, the discharge is considered to be continuous due to the fact that the time between discharges is negligible with respect to the lifetime of the plasma. To account for this apparent continuity, an extension of equation (9) is used to describe the volume based concentration of species i as a function of time. Thus, at n discharges into treatment, the concentration of the original contaminant molecule at any point in the reactor can be expressed as

$$C_{i_{na}} = \left(\frac{V_T + V_p}{V_T} \right) C_{i_{(n-1)\alpha}} = \left(\frac{V_T + V_p}{V_T} \right)^n C_o, \quad (10)$$

where n is the number of arc events in the DMPR and α , equal to 1 ms, is a time constant associated with the reactor. Recognizing that the total treatment time is equal to the number of arc events multiplied by the time constant ($t = n\alpha$), and taking the derivative of the species concentration with respect to time, yields the time dependence of the species concentration as a result of losses associated with the plasma:

$$(r_i)_{\text{plasma}} = C_{i_0} \frac{\ln(1 - V_p/V_T)}{\alpha} \exp\left(\frac{\ln(1 - V_p/V_T)}{\alpha} t\right). \quad (11)$$

Combining equations (4), (7) and (11) yields the following species conservation equation applicable to the DMPR:

$$\frac{dC_i}{dt} = -k_{\text{mt}} C_i^2 + C_{i_0} \frac{\ln(1 - V_p/V_T)}{\alpha} \times \exp\left(\frac{\ln(1 - V_p/V_T)}{\alpha} t\right) - k_{\text{DP}}. \quad (12)$$

Nonlinear least squares analysis and experimental data from Johnson *et al* [24] are utilized in conjunction with MATLAB[®] optimization routines to determine a and k_{DP} , and these parameters are, in turn, used in the CFD simulations.

3.1. Species balance optimization

Nonlinear least squares analysis is performed to obtain initial estimates for the plasma volume and zero-order rate constant associated with degradation due to photochemical processes. The accumulation and second-order loss terms in equation (12) are calculated from the experimental data and grouped

together to facilitate the convergence of the analysis routine. The result is

$$y = \frac{dC_i}{dt} + k_{\text{mt}} C_i^2 = C_{i_0} \frac{\ln a}{\alpha} \exp\left(\frac{\ln a}{\alpha} t\right) - k_{\text{DP}}, \quad (13)$$

where $a = (1 - V_p/V_T)$. An error function (equation (14))

$$E_{\text{min}} = \sum_{i=1}^N \left(\frac{\ln a}{\alpha} \exp\left(\frac{\ln a}{\alpha} t_i\right) C_o - k_{\text{DP}} - y_i \right)^2 \quad (14)$$

is generated that must be minimized while the partial derivatives of the error function with respect to k_{DP} (equation (15)) and with respect to a (equation (16)) are forced to zero:

$$\frac{\partial E}{\partial k_{\text{DP}}} = \sum_{i=1}^N \left(\frac{\ln a}{\alpha} \exp\left(\frac{\ln a}{\alpha} t_i\right) C_o - k_{\text{DP}} - y_i \right) = 0, \quad (15)$$

$$\frac{\partial E}{\partial a} = \sum_{i=1}^N \left\{ \left(\frac{\ln a}{\alpha} \exp\left(\frac{\ln a}{\alpha} t_i\right) C_o - k_{\text{DP}} - y_i \right) \times \left(\frac{C_o}{a\alpha} \exp\left(\frac{\ln a}{\alpha} t_i\right) \right) \left(1 + \left(\frac{\ln a}{\alpha} t_i \right) \right) \right\} = 0. \quad (16)$$

The estimated values of a and k_{DP} are incorporated into MATLAB[®] optimization routines for further analysis.

Equation (12) and the experimental data collected by Johnson *et al* [24] are analysed further utilizing MATLAB[®] optimization algorithms to incorporate additional constraints and information related to the behaviour of the attenuation processes in the DMPR. First, the molar density of the contaminant species is required to approach zero at long treatment times. Second, k_{mt} , which is calculated from experimental data (see figure 2), is allowed to decrease in the optimization routine; thereby giving the model the flexibility to account for the fact that the interphase mass transfer is driven by the magnitude of the concentration gradient across the gas-liquid interface. Data collected from the interphase mass transfer control experiments only account for losses in the liquid phase due to the volatility of MTBE. However, when depletion of the contaminant in the liquid phase is also occurring by photochemical and plasma loss mechanisms, the species attenuates more rapidly, resulting in a significant decrease in the interphase mass transfer driving force. Thus, the interphase mass transfer control experiments represent the maximum rate at which the volatile species can be removed by this mechanism, and is therefore used as an initial guess and upper bound for the subsequent optimization analysis.

The combination of nonlinear least squares analysis and MATLAB[®] optimization techniques yields the zero-order rate constant associated with direct photolysis, the second-order interphase mass transfer rate coefficient and the plasma volume. Predicted concentration profiles for the loss of each species due to interphase mass transfer and the plasma, as well as the nonlinear least squares fit to the experimental data from Johnson *et al* [24] for the combination of the two processes, are plotted in figure 3. As shown in the figure, attenuation of MTBE by the plasma is the major loss process, despite the fact that only approximately 10 μl of the 250 ml liquid solution is predicted to be promoted to the plasma state. Due to the

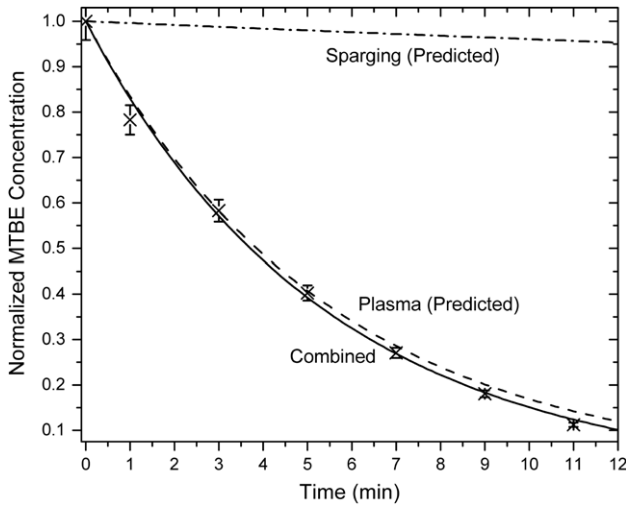


Figure 3. Plots of the normalized MTBE concentration as a function of time due to losses associated with the interphase mass transfer (— · —), the plasma (- - -) and a combination of the attenuation processes (—) as well as experimental data (×) collected from Johnson *et al* [24].

decrease in the driving force for the interphase mass transfer, sparging is predicted to play a minimal role in the removal process, with a rate constant of $0.01 \text{ mM}^{-1} \text{ min}^{-1}$, which is approximately an order of magnitude lower than the value calculated from the control experiments. With respect to direct photolysis, the rate of change of the MTBE concentration is not affected by this loss mechanism. This result is anticipated because photochemical degradation rates are negligible in solutions with a low conductivity. The experiments performed utilizing the DMPR were carried out with MTBE solvated in Millipore water generated by a Milli-Q ultrapure water system, resulting in solvent conductivities on the order of $10 \mu\text{S cm}^{-1}$. Also, the discharge in the DMPR occurs in a location where a significant portion, approximately 85%, of the bulk solution is shielded from the radiation emitted from the discharge. The information gathered from the above analysis is incorporated into the CFD simulations in an effort to provide qualitative and quantitative results regarding the fluid flow and reaction kinetics in the DMPR.

4. 3D Computation Fluid Dynamics simulations

FLUENT[®], a commercial CFD software package, is used to model flow characteristics and fluid pressure for both the original and coaxial DMPR configurations. The motivation behind modelling the two configurations, for which the computational grid is shown in figure 4, is to provide an insight into the velocity and pressure fields in the vicinity of the plasma for the experimental conditions reported by Johnson *et al* [24]. The original configuration model simulates fluid flow in the DMPR resulting from the rotation of the pin array. The central channel in the stationary electrode is not utilized in this configuration and thus the bulk fluid is only cycled through the electrode gap due to centrifugal forces created by the rotation of the array. The coaxial configuration model simulates fluid flow in the DMPR due to the rotation of the pin array and bulk liquid pumped through the central cylinder into the region

between the pin array and stationary electrode. The primary objectives of these models are to quantify the volumetric flow rates through important regions of the reactor and predict flow characteristics and fluid properties in the vicinity of the plasma as a function of the pin array spin rate and reactor configuration.

The flow characteristics and fluid properties are predicted by constructing CFD grids of the DMPR and solving the governing equations at each node. The simulations modelled an incompressible fluid with a constant viscosity for both laminar and turbulent flow conditions utilizing a laminar viscous solver and turbulent solver based on the continuity and Navier–Stokes equations,

$$\nabla \cdot \mathbf{v} = 0, \quad (17)$$

$$\rho \left(\frac{\partial \mathbf{v}}{\partial t} + \nabla (\mathbf{v}\mathbf{v}) \right) = -\nabla p + \mu \nabla^2 \mathbf{v} + \rho \mathbf{g}, \quad (18)$$

where ρ is the fluid density, \mathbf{v} is the velocity vector, t is time, p is the pressure, μ is the dynamic viscosity and \mathbf{g} is gravity. The meshes generated for the CFD simulations, shown in figure 4, are structured and contain approximately 10^6 nodes encompassed in 318 and 319 grid zones for the original and coaxial configurations, respectively. The large number of zones is necessary to generate a structured mesh, which reduces the impact associated with round off errors, thereby facilitating the convergence of the simulations. These structured meshes also have the added benefit of reducing the time necessary to reach a solution. The node density is selected such that the converged solutions are independent of the grid. This is accomplished by increasing the node density, especially in the regions where large gradients exist, until the solution associated with the preceding node density is within 0.1% of the solution associated with the final grid. A node density gradient is applied to the meshes, resulting in a higher density near the walls to ensure accurate resolution of all derivatives. The convergence criteria for the steady state simulations are that the residuals in the continuity, momentum and energy equations must each fall below a value of 10^{-4} . Water is used as the fluid, with an initial temperature of 300 K. The reactor pressure is constant at 101.3 kPa. Adiabatic, no-slip boundary conditions are applied at all solid surfaces. To determine the flow regime as a function of spin rate, the transition from laminar to turbulent flow is based on tangential annular flow of a Newtonian fluid [26], resulting in a transition to turbulent flow at a much higher Reynolds number ($Re \#$) when compared with more classical systems such as flow through a pipe. For pin array spin rates of 500 rpm or less ($Re \# \leq 3.75 \times 10^4$), the laminar viscous solver is employed. However, to obtain an accurate velocity vector field for spin rates of 750 rpm and higher ($Re \# \geq 7.75 \times 10^4$), a more complicated model is needed to accurately simulate the turbulent flow conditions in the DMPR which inherently has a large variation of characteristic lengths ranging from the electrode gap (0.5 mm) to the diameter of the reactor chamber (approximately 650 mm). For these conditions, it has been reported that the RNG based $k-\epsilon$ turbulence model provides the best prediction of the flow field [28]. Additional information pertaining to the simulation and convergence processes is contained in the supplemental information.

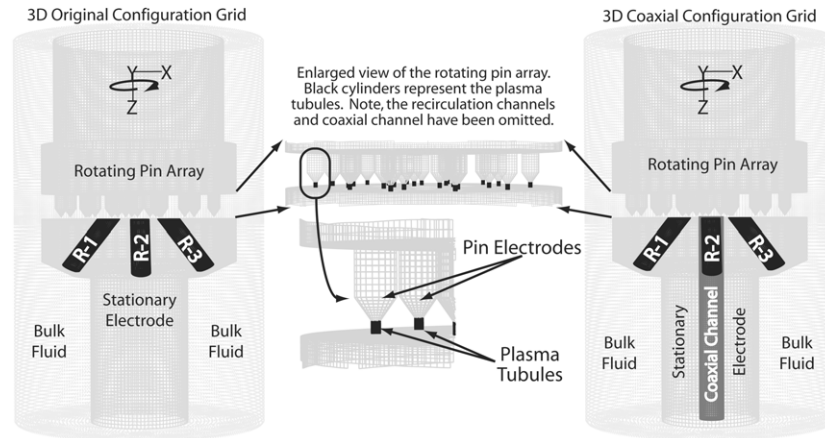


Figure 4. 3D CFD grids of the original and coaxial configurations. The recirculation channels, R-1, R-2 and R-3, are labelled along with the stationary electrode, rotating pin array, coaxial channel and bulk fluid. In all the CFD simulations, the pin array is spun clockwise. The grid zones assigned to simulate the plasma tubules were generated by evenly distributing the total plasma volume, as calculated by the nonlinear least squares and optimization analyses, among each of the 25 pin electrodes. The diameter of the pin array is approximately 50 mm while the gap between the stationary electrode surface and the top of the pin array, which can also be expressed as the sum of the electrode gap and length of a pin electrode, is approximately 6.5 mm.

4.1. Simulation results and discussion

The CFD simulations were performed on both the original and coaxial DMPR configurations to obtain qualitative and quantitative information concerning fluid flow and fluid properties as a function of pin array spin rate. To aid in the determination of the fluid flow rate through the individual plasma zones and the fluid pressure on the surface of each pin electrode, the recirculation channels and pin electrodes are labelled. Figure 5 illustrates the surface of the stationary electrode with the outlet of the recirculation channels labelled 1–3. The pin electrodes are projected onto the stationary electrode surface and subsequently labelled 1–25. The positions of the plasma zones with respect to the location of the recirculation channel outlets are consistent throughout each steady-state simulation. The data gathered from the simulations, along with figure 5, are first analysed to determine the volumetric flow rate of fluid through the plasma.

4.1.1. Velocity field analysis. Figure 6 contains bar graphs of the volumetric flow rate of the bulk liquid through the plasma in the original DMPR configuration for spin rates of 30, 1000, 2500 and 5000 rpm. As shown in the figure, the plasma zones generated from pins at larger radial distances from the centre experience higher radial volumetric flow rates than the plasma zones positioned towards the centre of the array. (As a reference, pins 11–14 correspond to the inner most plasma zones.) This prediction can be explained by the fact that the angular velocity component of the pins further away from the centre is larger and sweeps over a larger volume than a pin positioned towards the centre of the array, therefore yielding the symmetric profile of the bar graphs. A departure from this behaviour is observed with pin 8, for example, which has a higher flow rate through the plasma than some zones with a larger radial distance. The increased flow predicted for some of the inner plasma zones is due to their proximity to the recirculation channel outlets.

At 1000 rpm, the spin rate at which the original configuration experiments were performed, the total flow rate

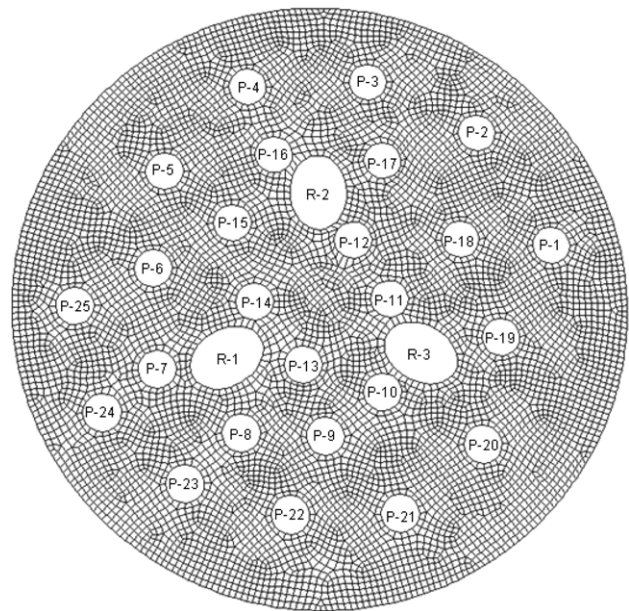


Figure 5. Location of the 25 pin electrodes (P-1–P-25) projected onto the surface of the stationary disc electrode and 3 recirculation channel outlets (R-1, R-2 and R-3) for the steady-state CFD simulations. The pin electrodes and recirculation channels have been labelled in order to compare fluid properties and the velocity field as a function of position in the DMPR.

through the recirculation channels and plasma is predicted to be 673 ml min^{-1} and 27 ml min^{-1} , respectively. While the rate of flow through the recirculation channels by centrifugal forcing provides adequate circulation of the reactor contents, corresponding to cycling the reactor fluid volume through the gap between the planar electrode surfaces approximately 2.7 times per minute, only 4% of the recirculated fluid comes into contact with the plasma. Thus, it would require approximately 9.3 min to cycle the same fluid volume through the plasma. Figure 7 contains plots of the flow rates through

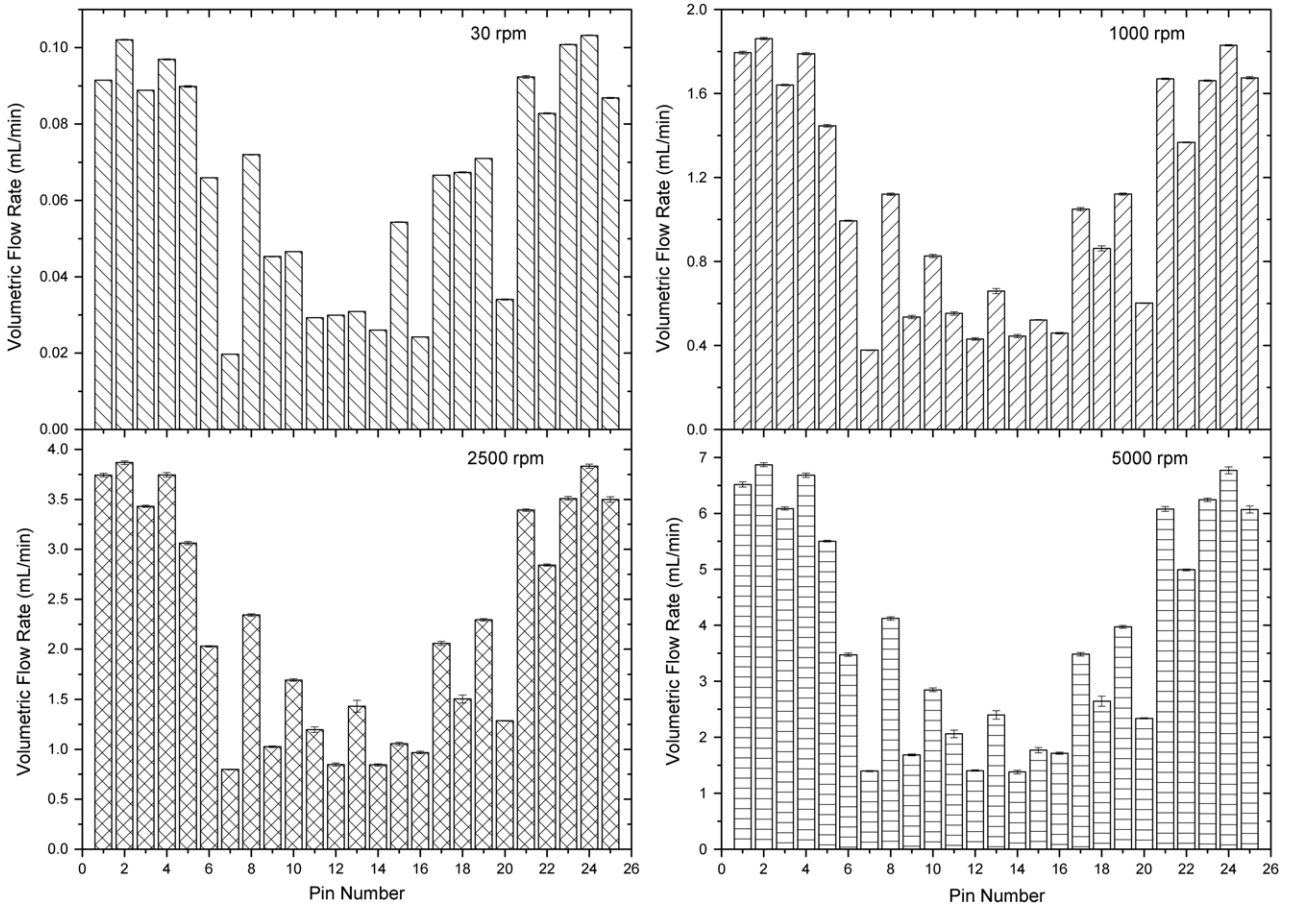


Figure 6. Bar graphs of the liquid volumetric flow rate through the plasma zones as a function of pin location for spin rates of 30, 1000, 2500 and 5000 rpm in an originally configured DMPR.

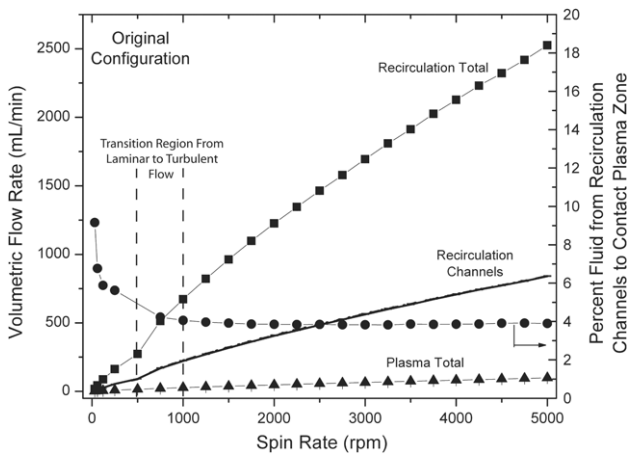


Figure 7. Plot of the individual recirculation channel flow rates, total recirculation channel flow rate (■) and total flow rate through the plasma (▲), left axis, as well as the percent of the total flow rate through the recirculation channels to contact the plasma (●), right axis, as a function of spin rate for the original configuration. Note: the individual recirculation channel flow rates are indistinguishable on this scale.

the recirculation channels and the grid volumes representing the plasma tubules, as well as the percent of the total flow rate passing through the recirculation channels that contacts the plasma, as a function of the spin rate for the original configuration. The percent of the total flow rate passing

through the recirculation channels that contacts the plasma is calculated by dividing the total fluid flow through the plasma zones by the total flow through the recirculation channels. As shown in figure 7, the fraction of the fluid travelling through the recirculation channels that contacts the plasma decreases with an increase in the flow rate for laminar flow conditions. However, for turbulent flow conditions, the percentage remains relatively constant at 4% and is not a function of the spin rate. The steady drop from approximately 9%, predicted at 30 rpm, to approximately 4%, predicted for spin rates associated with turbulent flow conditions, can be explained using the velocity vector plots contained in figure 8.

Velocity vectors in a plane bisecting recirculation channel 2 are plotted in figure 8 for spin rates of 30, 1000 and 5000 rpm. The CFD grids for the pin electrodes and stationary electrode are superimposed on the plane containing the velocity vectors for purposes of clarity. At 30 rpm, inertial forces of the fluid exiting the recirculating channel are relatively weak compared with the centrifugal forces produced by spinning the pin array. However, as the spin rate is increased, the fluid velocity exiting the recirculation channels also increases, resulting in the inertial forces that cause the exiting fluid to continue to the top of the pin array. As the fluid decelerates, centrifugal forces turn the flow radially, forcing the liquid out of the gap. Thus, at 30 rpm, a larger fraction of the fluid exiting the recirculation channels passes through the plasma zones than at higher spin rates. With respect to the fraction of fluid to contact the plasma

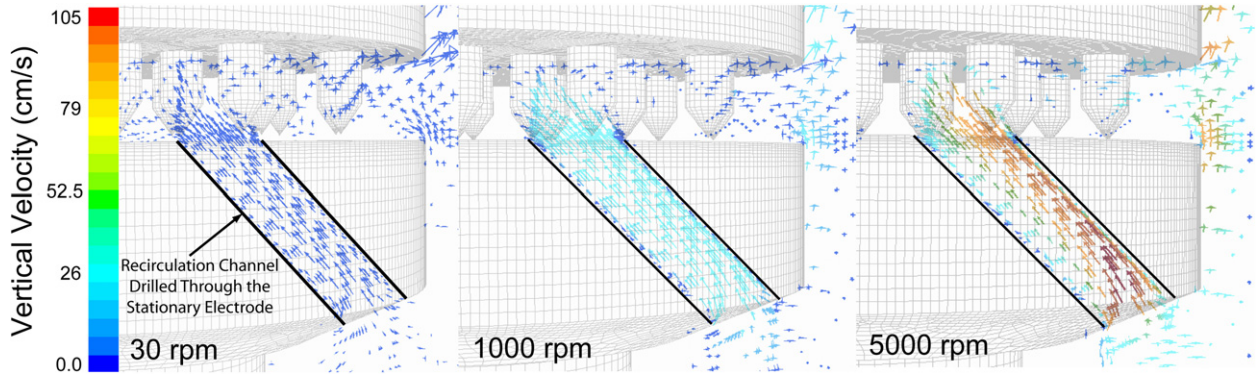


Figure 8. Plots of velocity vectors induced by pin array spin rates of 30, 1000 and 5000 rpm travelling in a vertical plane that bisects recirculation channel 2, for which the edges are outlined in black. As the spin rate increases, the velocity of the fluid also increases causing a large percentage of the fluid to bypass the plasma being generated at the electrode tips. The location of recirculation channel 2 within the reactor can be found in figure 4.

being constant for turbulent flow conditions, the simulations predict a comparable, monotonic increase of both the rate at which the fluid flows through the recirculation channels and the plasma, resulting in a contact percent that is not a function of the spin rate. Trends similar to that predicted for the original configuration are also predicted for the coaxial configuration.

To compare the simulation results from the original configuration to that of the coaxial configuration, a similar analysis is performed on the coaxial model CFD data. As in the simulations conducted on the original configurations, the symmetric behaviour exhibited in figure 6 is also predicted because of the larger angular velocity component of the pins further away from the centre (not shown). Cycling bulk fluid through the centre of the stationary electrode does not qualitatively alter this aspect of the velocity field when compared with the original configuration. Departures from this behaviour are again predicted for some of the plasma zones due to their proximity to the recirculation channel outlets. At 500 and 1000 rpm, the spin rates at which the coaxial configuration experiments were performed, the total flow rate through the plasma is predicted to be 15 and 26 ml/min, while the combined total flow rate through the recirculation and coaxial channels is 378 ml min⁻¹ and 776 ml min⁻¹, respectively. Although the recirculation of the bulk fluid through the gap between the pin array and stationary electrode is again adequate in the coaxial configuration, only 3.5% and 4% of the cycled fluid at 500 rpm and 1000 rpm, respectively, contacts the plasma. Thus, it would require approximately 17 min and 9.6 min, respectively, to cycle the same fluid volume through the plasma for spin rates of 500 and 1000 rpm. Figure 9 displays the flow rates through the coaxial channel, recirculation channels and the plasma, as well as the percent of the total flow rate through the gap between the pin array and stationary electrode to contact the plasma, as a function of the spin rate for the coaxial configuration. The fraction of fluid travelling through the channels that contacts the plasma increases with an increase in the spin rate for laminar flow conditions. For turbulent flow, however, the percentage remains relatively constant at 3.75%, again leading to the conclusion that the contact fraction, if not independent, is a weak function of the spin rate. The increase from 1.15% at 30 rpm to 3.75% for spin rates consistent with turbulent flow may again be explained utilizing velocity vector plots similar to those produced for the original configuration.

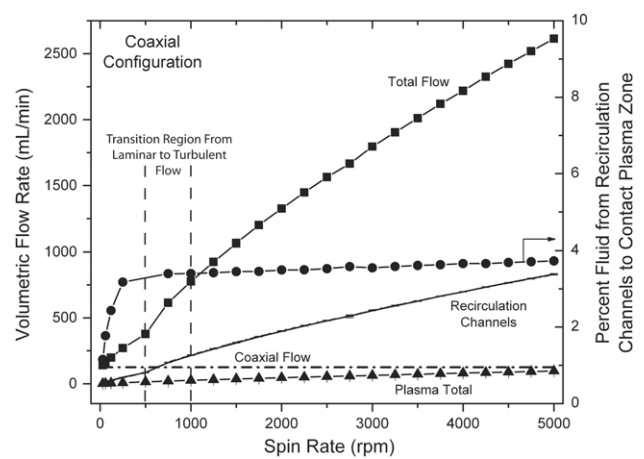


Figure 9. Plot of the individual recirculation channel flow rates, coaxial channel flow rate (— · —), total flow rate through the gap between the pin array and stationary electrode (■), i.e. the sum of the recirculation channels and coaxial channel flow rates, and total flow rate through the plasma (▲), left axis, as well as the percent of the total flow rate through the recirculation channels to contact the plasma (●), right axis, as a function of spin rate for the coaxial configuration. Note: the individual recirculation channel flow rates are indistinguishable on this scale.

Velocity vectors for a plane bisecting recirculation channel 2 and the coaxial channel are analysed for spin rates of 30, 1000, 2500 and 5000 rpm (not shown). The analysis demonstrates that the induced volumetric flow rate of 5 ml min⁻¹ from each of the recirculation channels at 30 rpm is very small compared with the pump-driven flow rate of 125 ml min⁻¹ through the coaxial channel. The combination of the relatively large vertical velocity component of the fluid exiting the coaxial channel and its location at the point of minimum (zero) centrifugal, leads to most (98.9%) of the fluid passing above the plasma as it travels across the pin electrode array. Thus, the flow in the coaxial configuration at 30 rpm is dominated by the external pump, whereas at higher spin rates the flow contribution of the external pump to the overall velocity field becomes less important compared with the contribution of the spinning pin array. As the pin array spin rate is increased, the centrifugal forces play an increasingly dominant role in the velocity field, resulting in an increase in the plasma contact fraction, as shown in figure 9.

As the flow becomes turbulent, the plasma contact fraction becomes less dependent on the spin rate until the flow exiting the recirculation channels dominates any contribution made by the external pump to the velocity field. At that point, the plasma contact fraction, as previously seen in the original configuration, is no longer a function of the spin rate. As in the original configuration, this can be attributed to the monotonic increase in both the rate at which the fluid flows through the recirculation channels and the plasma.

4.1.2. Fluid pressure analysis. The minimum applied potential required to initiate an arc discharge in a point-to-plane electrode configuration is correlated with minimizing the radius of curvature of the pin electrode, which results in the maximum electric field strength for the given potential. In the DMPR, which employs a point-to-plane electrode configuration, the pin electrodes are mechanically sharpened at an angle of 30° to capitalize on the lower power requirements commensurate with sharper pin tips. It is observed experimentally, however, that when the array is spun, the plasma discharge originates from an area of the pin electrode surface that does not correspond to the minimum radius of curvature. To explain this observed behaviour, the CFD simulation data for both the original and the coaxial configurations are analysed to determine to what degree the fluid pressure is a function of position in the DMPR, thereby focusing the location of the discharge to a distinct region of the pin electrode surface for which the electric field strength is not maximized.

Static pressure contour plots of the pin electrode surfaces in the original DMPR configuration are shown in supplementary figure S2 for pin array spin rates of 30, 1000 and 5000 rpm. As illustrated in the figure, pressure gradients develop for spin rates as low as 30 rpm and become more pronounced as the spin rate is increased. The maximum pressure difference predicted by the simulations for 30 rpm, 1000 rpm and 5000 rpm are approximately 2.5 Pa, 460 Pa, and 6300 Pa, respectively. The contours generated by the simulations also demonstrate that the minimum pressure occurs on the rear (downstream) surfaces of the pin electrodes. This behaviour can be explained utilizing figure 10, which contains a contour plot of the total pressure in the original DMPR in the horizontal plane 1 mm above the stationary electrode surface for a pin array spin rate of 2000 rpm. As the pin electrodes travel through the fluid in a clockwise direction, flow separation around the pin electrodes is predicted, resulting in a region of higher pressure on the front face and a stagnation region of lower pressure along the back face. The rear stagnation regions predicted by the simulations correspond to the areas where the plasma discharge is experimentally observed to originate, but is not, however, the region on the pin electrode surface for which the electric field strength is maximized. The origination of the plasma arcs from a region of lower pressure can be explained using the Paschen curve.

The Paschen curve relates the breakdown voltage to the product of the pressure and electrode gap for a given electrode geometry and discharge conditions. The segment of the curve with a negative slope describes the breakdown behaviour of gases at pressures considerably below atmospheric pressure. As the pressure between the electrodes is reduced, the

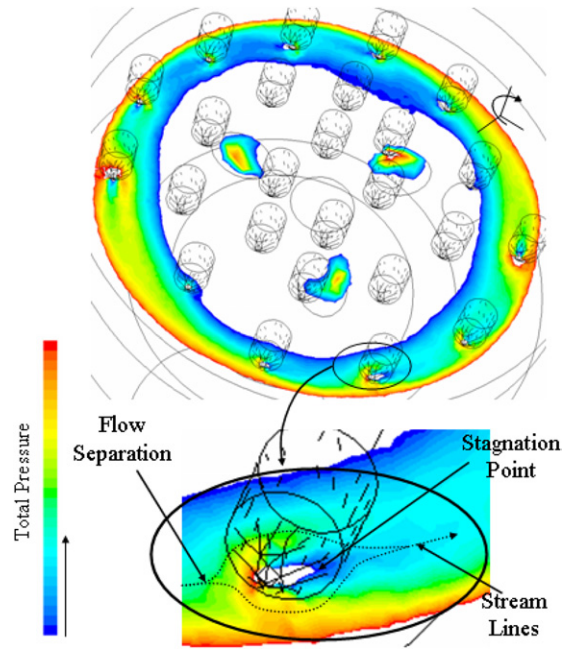


Figure 10. Pressure contours generated by a pin array spin rate of 2000 rpm in the original configuration from a horizontal plane 1 mm into the gap between the stationary electrode surface and the pin array. The 1 mm distance is measured from the stationary electrode surface. Evidence of flow separation and a stagnation region is also presented. Note: the rotation of the pin array is defined as clockwise.

breakdown of the gas becomes more difficult to initiate, that is, a higher applied potential is needed due to the fact that the gap is devoid of molecules with which electrons emitted from the electrodes can collide and thus generate a plasma. However, as the pressure is increased for a specified electrode gap, the curve passes through a minimum and the slope becomes positive. This is the region of the curve applied to plasmas initiated at approximately atmospheric pressure and is thus applicable to the plasma generated in the DMPR. The curve therefore predicts that as the fluid pressure decreases, the potential drop across the electrodes required to initiate an arc discharge in the DMPR also decreases. Thus, for the experimental conditions employed by Johnson *et al* [24], the reduction in fluid pressure adjacent to the pin electrode surface due to spinning the pin array is sufficient to compensate for the larger electric field strength at the pin tip when initiating an arc discharge. The distance above the stationary electrode surface for which the pin electrode surface pressure is a minimum for a given pin location and spin rate is therefore analysed to ascertain the possible increase in the distance travelled by the plasma arcs.

As dictated by the Paschen curve, an increase in the electrode gap requires an increase in the breakdown voltage to initiate a discharge, assuming the pressure remains constant. The CFD simulations predict that a discharge originating from the point of minimum pressure results in an increase in the electrode gap of $83 \mu\text{m}$ for a majority of the pin electrodes. In some cases such as pin 7, however, an increase of approximately $450 \mu\text{m}$ is predicted. Such a substantial increase in the distance from the stationary electrode for which the surface pressure is minimized for positions corresponding to pins 6, 7, 10, 11, 13 and 14 can be attributed to their location with respect to the recirculation channel outlets.

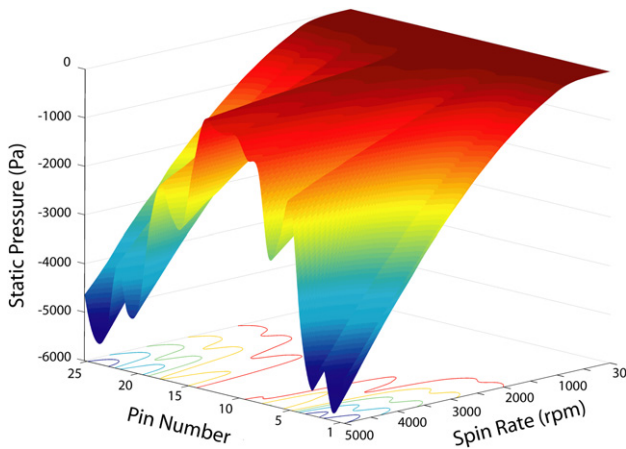


Figure 11. Surface plot of the minimum static pressure predicted by the CFD simulations on the pin electrode surface in the original configuration as a function of pin number and spin rate. The minimum pressure increases with an increase in the spin rate and radial distance from the centre of the pin array due to an increase in angular velocity.

The close proximity of the pins to the outlets may result in varying fluid conditions due to the contribution of the bulk fluid exiting the recirculation channels. However, pins 8, 9 and 12 do not demonstrate this behaviour, suggesting that the uncharacteristically large increase in the distance from the stationary electrode surface ($450\ \mu\text{m}$) occurs predominately when the vertical and radial velocity components of fluid exiting the recirculation channels affects the pin electrode surface conditions. While it has been shown that an increase in the pin array spin rate invokes a pressure gradient along the pin electrode surface, the simulations also predict a comparable increase in the magnitude of the pressure gradient with an increase in the radial distance from the centre of the pin array.

The increase in the pressure gradient along the pin electrode surface is due to the increase in the magnitude of the angular velocity with distance from the centre. To determine the effect of pin position on the minimum pressure, a surface plot of the minimum static pressure as a function of radial position and spin rate is shown in figure 11. The radial distance for each spiral strand of pin electrodes, illustrated in figure 5, increases from the middle of the surface plot, pins 12 and 13, to the edges, pins 1 and 25. As illustrated by the surface plot, the minimum pressure does not appear to be a strong function of radial position at lower spin rates. As the spin rate increases, however, the change in the minimum pin electrode surface pressure as a function of radial position becomes appreciable. In fact, the decrease in pressure due to an increase in radial position is comparable to the decrease resulting from an increase in spin rate. The symmetric nature of the surface plot is due to the fact that the pins in the centre of the surface plot also correspond to the innermost pin positions. The surface plot presented in figure 11 is not truly symmetric about the two inner most pins due to the bulk liquid exiting the recirculation channels and the close vicinity of a number of the pin electrodes to the recirculation channel outlets. To perform a more quantitative analysis on the changes in pressure as a function of radial position and spin rate, the radial position and minimum pressure predicted by the simulations are analysed further.

The change in the minimum surface pressure from the inner most to the outer most pin for spin rates of 30 rpm, 1000 rpm, 2500 rpm and 5000 rpm are 2.0 Pa, 447 Pa, 1914 Pa and 5382 Pa, respectively. The differences in minimum surface pressure from the inner pins to the outer pins are consistent with experimental observations relating an increased sputtering rate to pins with larger radial distance. As predicted at higher spin rates, the change in pressure as a function of pin location is comparable to changes resulting from an increase in spin rate. For example, an increase from 30 to 5000 rpm results in a pressure change of 5846 Pa for pin 2, whereas the maximum pressure change due to an increase in radial position at 5000 rpm is 5382 Pa. Thus, the comparable changes in the pressure as a result of pin location and spin rate require both parameters to be considered when evaluating the discharge conditions. The pressure difference caused by pin location is more pronounced when considering increases in spin rate of only 250 rpm. Spin rate increases from 750 to 1000 rpm, 2250 to 2500 rpm and 4750 to 5000 rpm result in pressure changes of 184 Pa, 312 Pa and 402 Pa, respectively, all of which are lower than the pressure changes predicted as a result of an increase in the radial position. A similar analysis is performed on the data gathered from the coaxial model simulations to determine if the trends predicted for the original configuration are consistent with the coaxial configuration.

Static pressure contour plots of the pin electrode surface in the coaxial DMPR configuration are displayed in supplementary figure S3 for pin array spin rates of 30, 1000 and 5000 rpm. In contrast to what is predicted for the original DMPR configuration, pressure gradients do not appear to develop on the surface of the pin electrodes at spin rates near 30 rpm. As illustrated in supplementary figure S3, the flow at 30 rpm is dominated by a pressure drop across the x - y plane due to the external pump driving fluid into the reactor through the middle of the stationary electrode. As the spin rate increases, however, the flow generated by the external pump becomes less important when compared with the flow generated by the spinning pin array, resulting in pressure gradients on the pin electrode surfaces, which, as in the original configuration, become more pronounced as the spin rate increases. The maximum pressure difference predicted by the simulations for 30 rpm, 1000 rpm, and 5000 rpm are approximately 12 Pa, 450 Pa, and 6400 Pa, respectively. The pressure values are similar to those predicted for the original configuration at 1000 and 5000 rpm. This result is consistent with the fact that as the spin rate increases, the effect of the external pump on the velocity field decreases. As in the original configuration, the simulations predict the minimum pressure to occur on the rear surfaces of the pin electrodes. This behaviour is attributed to the same mechanisms discussed previously for the original configuration. The distance above the stationary electrode surface for which the pressure is minimized is also investigated to determine a possible increase in the electrode gap.

The coaxial CFD simulations predict that a discharge originating from the point of minimum pressure results in an increase of $82\ \mu\text{m}$ in the electrode gap for a majority of the pin electrodes. As seen in the original configuration for pin electrodes in close proximity to the recirculation channel outlets, substantial increases are predicted for pins 6, 7, 10, 11, 13 and 14, but not for the other pins at similar radial

positions. To determine the effect of pin position on the minimum pressure, a surface plot (not shown) of the minimum static pressure as a function of radial position and spin rate, similar to the plot generated from the original configuration data, is analysed. As predicted for the original configuration, the minimum pressure does not appear to be a strong function of radial position at lower spin rates. The same behaviour and trends present in the original configuration surface plot, such as the symmetric nature of the surface and changes in the minimum pin electrode surface pressure as a function of radial position, are apparent for the coaxial configuration as well. A more quantitative analysis on the changes in pressure as a function of radial position and spin rate is performed utilizing data obtained from the simulations.

The maximum change in the minimum surface pressure as a function of pin location for spin rates of 30 rpm, 1000 rpm, 2500 rpm and 5000 rpm are 1.9 Pa, 439 Pa, 1902 Pa and 5408 Pa, respectively, in the coaxial configuration. The changes in pressure are almost identical to those predicted for the original configuration, even at 30 rpm where it has been previously shown that the overall fluid flow in the DMPR is dominated by the external pump. This can be explained by the fact that the velocity of the fluid exiting the coaxial channel is such that it bypasses the plasma zones, and thus the pin electrodes tips, in a manner similar to that predicted for the bulk fluid exiting the recirculation channels at high pin array spin rates. As predicted for the original configuration, the change in pressure due to pin location is comparable to changes resulting from an increase in spin rate. For example, an increase from 30 to 5000 rpm results in a pressure change of 5889 Pa for pin 2, whereas the maximum pressure change due to an increase in radial position at 5000 rpm is 5408 Pa. As in the original configuration, it is therefore important to consider both pin location and spin rate when evaluating the discharge conditions.

5. Conclusion

The CFD simulations of the original and coaxial configurations yielded qualitative and quantitative results relating the fluid flow and the fluid pressure to the reactor parameters such as pin array spin rate and pin location. The simulations predict a region of low pressure on the rear surfaces of the pin electrodes, where the pressure decreases with increasing spin rate. The reduced pressure on the pin electrode surface resulting from an increase in spin rate allows an increase in the electrode gap while maintaining a constant voltage drop. Thus, increasing the spin rate above that utilized by Johnson *et al* [24] would allow an increase in the electrode gap while still employing an applied potential of approximately 200 V. The increase in the electrode gap will reduce the residence time required to treat the given amount of fluid in the DMPR by increasing the plasma volume. The fact that the plasma arc originates from a region on the pin electrode surface corresponding to the lowest pressure and not the highest electric field strength demonstrates that reducing the radius of curvature by mechanical and/or electrochemical processes is unnecessary if an appreciable reduction in the pin electrode surface pressure can be achieved. Thus, innovative approaches to further reduce the surface pressure in addition to increasing the spin rate should be sought

to further reduce the power requirements of the DMPR. The change in the minimum pressure as a function of pin location also has implications for the scalability of the DMPR.

The pin electrode surface pressure dependence on radial position dictates that the diameter of the pin array, and thus the number of pin electrodes that can be incorporated into the DMPR, is finite. This limit is due to the fact that, as the minimum pressure decreases, the impedance of the fluid between the pin electrodes and the surface of the stationary electrode also decreases. Thus, pins located at the centre of the array will experience a higher impedance when compared with pins with a larger angular velocity. The differences in electric field strength will result in an inability to initiate or sustain a plasma discharge on the innermost pins. To counteract this limitation in an effort to increase the fluid volume that can be treated by a DMPR, it is important to develop an electrode configuration that generates a consistent angular velocity regardless of radial position. Another option is to design a conical pin array in which the electrode gap increases with an increase in radial position to compensate for the decrease in pressure.

References

- [1] Goheen S C, Durhlan D E, McCulloh M and Heat W O 1992 *Proc. 2nd Int. Symp. on Chemical Oxidation (Nashville, TN, USA)* pp 356–67
- [2] Hoeben W F L M, van Veldhuizen E M, Rutgers W R and Kroesen G M W 1999 *J. Phys. D: Appl. Phys.* **32** L133–9
- [3] Hayashi D, Hoeben W F L M, Dooms G, van Veldhuizen E M, Rutgers W R and Kroesen G M W 2000 *J. Phys. D: Appl. Phys.* **33** 2769–74
- [4] Hoeben W F L M, van Veldhuizen E M, Rutgers W R, Cramers C A M G and Kroesen G M W 2000 *Plasma Sources Sci. Technol.* **9** 361–9
- [5] Sun B, Sato M and Clements J S 1997 *J. Electrostat.* **39** 189–202
- [6] Willberg D M, Lang P S, Hochemer R H, Kratel A and Hoffmann M R 1996 *Environ. Sci. Technol.* **30** 2526–34
- [7] Sun B, Sato M and Clements J S 1999 *J. Phys. D: Appl. Phys.* **32** 1908–15
- [8] Sun B, Sato M, Harano A and Clements J S 1998 *J. Electrostat.* **43** 115–26
- [9] Sunka P, Babicky V, Clupek M, Lukes P, Simek M, Schmidt J and Cernak M 1999 *Plasma Sources Sci. Technol.* **8** 258–65
- [10] Joshi A A, Locke B R, Arce P and Finney W C 1995 *J. Hazard. Mater.* **41** 3–30
- [11] Lang P S, Ching W K, Willberg D M and Hoffmann M R 1998 *Environ. Sci. Technol.* **32** 3142–8
- [12] Lisitsyn I V, Nomiya H, Katsuki S and Akiyama H 1999 *Rev. Sci. Instrum.* **70** 3457–62
- [13] Malik M A, Ghaffar A and Malik S A 2001 *Plasma Sources Sci. Technol.* **10** 82–91
- [14] Mikula M, Panak J and Dvonka V 1997 *Plasma Sources Sci. Technol.* **6** 179–84
- [15] Sharma A K, Locke B R, Arce P and Finney W C 1993 *Hazard. Waste Hazard. Mater.* **10** 209–19
- [16] Shin W T, Yiacoymi S, Tsouris C and Dai S 2000 *Indust. Eng. Chem. Res.* **39** 4408–14
- [17] Sun B, Sato M and Clements J S 2000 *Environ. Sci. Technol.* **34** 509–13
- [18] Wen Y and Jiang X 2000 *Plasma Chem. Plasma Process.* **20** 343–51
- [19] Willberg D M, Lang P S, Hochemer R H, Kratel A W, Hoffmann M R 1996 *Chemtech* **26** 52–7
- [20] Denes F S and Young R A 1996 Apparatus for reactions in dense-medium plasmas *US Patent # 5,534,232*

- [21] Denes F S, Manolache S O and Hershkowitz N 2002 Method and apparatus for producing colloidal nanoparticles in a dense medium plasma *US Patent Application #* 20020037320
- [22] Manolache S, Somers E B, Wong A C L, Shamamian V and Denes F 2001 *Environ. Sci. Technol.* **35** 3780–5
- [23] Manolache S O, Shamamian V A and Denes F 2004 *J. Environ. Eng.* **130** 17–25
- [24] Johnson D C, Shamamian V A, Callahan J H, Denes F S, Manolache S O and Dandy D S 2003 *Environ. Sci. Technol.* **37** 4804–10
- [25] Roth J R 1995 *Industrial Plasma Engineering Vol. 1: Principles* (Bristol, UK: Institute of Physics Publishing)
- [26] Bird R B, Stewart W E and Lightfoot E N 1960 *Transport Phenomena* (New York: Wiley)
- [27] Hirschfelder J O, Curtiss C F and Bird R B 1954 *Molecular Theory of Gases and Liquids* (New York: Wiley)
- [28] Choudhury D 1993 Introduction to the renormalization group method and turbulence modeling *Fluent Inc. Technical Memorandum* TM-107